

# Disentangling the dynamics of transient spin and orbital magnetization in SrTiO<sub>3</sub> via the inverse Faraday effect from RT-TDDFT

Andri Darmawan, Markus E. Gruner, and Rossitza Pentcheva  
*Department of Physics and Center for Nanointegration (CENIDE),  
 Universität Duisburg-Essen, Lotharstr. 1, 47057 Duisburg, Germany*  
 (Dated: February 25, 2026)

Light-matter interaction allows to achieve non-equilibrium states that are otherwise inaccessible. Motivated by recent experiments that report ferroelectricity – and even multiferroicity – in the prototypical diamagnetic band insulator SrTiO<sub>3</sub> induced by terahertz pulses, we investigate the carrier and magnetization dynamics of SrTiO<sub>3</sub> excited optically by linearly and circularly polarized light. Our real-time time-dependent density-functional theory (RT-TDDFT) results reveal a highly non-trivial, site- and orbital-dependent temporal evolution with charge transferred from O 2*p* to Ti 3*d* states. For linearly polarized light the orbitally polarized lobes of electron density at the oxygen and titanium sites fluctuate out-of-phase, resembling the soft transverse optical phonon mode, dynamically breaking inversion symmetry. In contrast, circularly polarized pulses induce a coherent rotation of the charge dipoles around O. This induces a helicity-dependent finite transient magnetization with opposite sign for oxygen and Ti even without ionic motion. Detailed analysis reveals that the dominant mechanism is the transfer of angular momentum of light to the electronic orbital angular momentum, while spin-orbit coupling plays a key role in the transfer from orbital to spin angular momentum, the former being an order of magnitude larger than the latter.

*Introduction*—Preparation and manipulation of transient magnetic states with light has proven its potential as a powerful route towards novel applications, with ultrafast writing processes for magnetic storage technologies as a prominent example [1–4]. The seminal work of Beaupaire *et al.* [5] demonstrated the demagnetization of metallic ferromagnets by a single femtosecond laser pulse, paving the way for intensive reasearch on laser-induced phenomena in diverse classes of materials [6–8]. In this context, real-time time-dependent density-functional theory (RT-TDDFT) has become a tool of choice for modeling a broad spectrum of light-induced phenomena, including carrier dynamics in 2D materials [9], heterostructures [10–12], Weyl-semimetals [13] and non-magnetic semiconductors [14] and has provided detailed insights into the redistribution of spin and orbital angular momentum during demagnetization [15–17]. For example, the optically induced intersite spin transfer (OISTR) [18] was shown to generate a transient ferromagnetic contribution in otherwise antiferromagnetic multicomponent systems or heterostructures.

The ultrafast demagnetization upon optical absorption of linearly polarized light (LPL) is commonly related to thermal effects [5, 15, 17, 19]. In contrast, the interaction of circularly polarized light (CPL) with materials allows for nonthermal excitations via the inverse Faraday effect (IFE), where a time-dependent electric field induces an effective magnetic field [20]. Originally described in terms of classical electrodynamics [20–22], extensions were introduced to account for absorbing media, spin-polarized systems, ultrafast pulses [23, 24]. Material-specific quantum-mechanical formulations [25, 26] revealed distinct spin- and orbital-related contributions in metals that depend sensitively on material and

photon energy [27]. IFE has been discussed for various materials including semimetals [28], (non)magnetic metals [27] or Mott insulators [29]. An intriguing possibility is to induce magnetization in nonmagnetic semiconducting or insulating materials, as recently reported for 2D materials, MoS<sub>2</sub> [30], BiH [31] or oxides V<sub>2</sub>O<sub>5</sub> [32].

SrTiO<sub>3</sub> (STO) is a diamagnetic insulator [33] and a prototypical quantum paraelectric where quantum fluctuations suppress the ferroelectric (FE) transition [34]. STO can become superconducting upon doping [35] and serves as a versatile substrate for complex oxide electronics [36], hosting a two-dimensional electron gas at interfaces e.g. with LaAlO<sub>3</sub> [37] and also on its bare surface [38, 39]. The structural and electronic properties of bulk STO have been extensively characterized with DFT [40–43], while many-body perturbation theory provides accurate optical and X-ray absorption spectra [44–46]. Recent experiments have demonstrated that linearly polarized light (LPL) with mid-infrared [47] and THz [48] frequencies can transiently induce ferroelectricity in STO, supported by RT-TDDFT simulations of THz [49] or optical excitations [50]. Beyond transient FE effects, Basini *et al.* showed that circularly polarized THz pulses can induce multiferroicity in STO by exciting infrared phonon modes [51]. The effect was attributed to the phonon analogue of the IFE – the Barnett effect – where coherent phonon motion induces a transient magnetization. This dynamical multiferroicity [52] was linked to chiral phonons [53] excited by CPL. Several theoretical approaches have been put forward to explain the experimental observation [51] from different perspectives including second order perturbation theory with electron phonon coupling [54], non-Maxwellian fields [55, 56], electron-nuclear quantum geometry [57] and atomic orbital magnetization [58]. So far, the light-induced magne-

tization in STO has been limited to THz phonon excitation; to our knowledge, optically excited magnetisation by circularly polarized light has not been addressed so far.

In this work, we investigate the carrier and magnetization dynamics of STO under optical excitation with both linearly (LPL) and circularly polarized light (CPL) using RT-TDDFT. By systematically varying the laser frequency and fluence we reveal a highly non-trivial site- and orbital-dependent carrier dynamics in the excited state, with anti-phase charge fluctuations at the oxygen and titanium sites for linear polarization reminiscent of the soft transverse optical phonon mode. Most importantly, CPL in the optical frequency range generates a rotation of the charge dipoles around O and a sizable transient magnetic moment even without the prior excitation of phonon modes. Our results shed light on the underlying mechanism with light helicity transferred to the electronic orbital angular momentum, while spin-orbit coupling turns out to be essential in inducing the substantially smaller spin contribution.

*Method*— To study the electronic and magnetic response of STO upon laser excitation, we performed RT-TDDFT calculations employing the Elk code [59] which implements the all-electron full-potential linearized augmented plane-wave (FP-LAPW) method. We used the generalized gradient approximation for the exchange correlation functional in the implementation of Perdew, Burke, and Ernzerhof (GGA-PBESol) [60]. The non-collinear time-dependent Kohn-Sham equations are solved to obtain the time-dependent spinors

$$i\frac{\partial\psi_j(\mathbf{r},t)}{\partial t} = \left[ \frac{1}{2} \left( -i\nabla + \frac{1}{c}\mathbf{A}_{\text{ext}}(t) \right)^2 + v_s(\mathbf{r},t) + \frac{1}{2c}\boldsymbol{\sigma}\cdot\mathbf{B}_s(\mathbf{r},t) + \frac{1}{4c^2}\boldsymbol{\sigma}\cdot(\nabla v_s(\mathbf{r},t)\times(-i\nabla)) \right] \psi_j(\mathbf{r},t), \quad (1)$$

where  $\boldsymbol{\sigma}$  is the vector of Pauli matrices. The effective Kohn-Sham (KS) potential  $v_s(\mathbf{r},t) = v_{\text{ext}}(\mathbf{r},t) + v_{\text{H}}(\mathbf{r},t) + v_{\text{xc}}(\mathbf{r},t)$  consists of the external potential  $v_{\text{ext}}$ , the Hartree potential  $v_{\text{H}}$ , and the exchange-correlation potential  $v_{\text{xc}}$ . The effective KS magnetic field  $\mathbf{B}_s(\mathbf{r},t) = \mathbf{B}_{\text{ext}}(\mathbf{r},t) + \mathbf{B}_{\text{xc}}(\mathbf{r},t)$ , contains the external magnetic field  $\mathbf{B}_{\text{ext}}$  and magnetic field stemming from the exchange-correlation potential  $\mathbf{B}_{\text{xc}}$ . The final term in Eq. 1 represents the spin-orbit coupling (SOC). We evaluate the total spin and orbital angular momentum by adding the contribution of each ion within the MT sphere.

The laser pulse is described by a vector potential  $\mathbf{A}_{\text{ext}}(t)$ , represented by a sinusoidal wave modulated by a Gaussian envelope function, within the dipole approximation. The electric field is obtained from the time-derivative of the vector potential,  $\mathbf{E} = -\frac{1}{c}\frac{\partial\mathbf{A}}{\partial t}$ . The linearly polarized pulse is modeled as  $\mathbf{A}_{\text{ext}}(t) = \mathbf{A}_0 \exp\left[-2\ln(2)\frac{(t-t_0)^2}{d^2}\right] \sin[\omega(t-t_0) + \phi]$ , where  $\mathbf{A}_0$  is

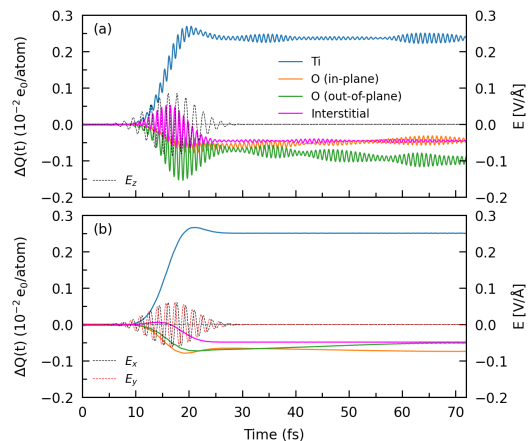


FIG. 1. Time evolution of the electronic charge  $\Delta Q = Q(t) - Q(0)$  within the muffin-tin spheres of Ti, O and interstitial region following an excitation with (a) linearly and (b) circularly polarized light with a laser frequency of  $\hbar\omega = 2.5$  eV, laser peak intensity of  $10^{11}$  W/cm<sup>2</sup> and a FWHM of 10 fs. The brown dashed line depicts the  $z$ -component of the electric field of LPL, while black and red dashed lines represent the  $x$ - and  $y$ -components of the electric field of CPL.

the vector polarization amplitude,  $t_0$  is the laser peak time,  $d$  is the full-width of half maximum (FWHM),  $\omega$  is the laser frequency, and  $\phi$  is the phase of the laser pulse. A circularly polarized pulse is modeled by a superposition of two linearly polarized pulses along  $x$  and  $y$  with a  $\pm\pi/2$  phase shift.

*Results*— We explore in a first step the charge dynamics of SrTiO<sub>3</sub> upon laser excitation using linearly and circularly polarized light. The former has an electric field in  $z$ -direction, whereas the electric field vectors of left- (LH) and right-handed (RH) CPL lie in the  $xy$ -plane. We used a photon energy of 2.5 eV which is above the PBESol band gap of 1.8 eV that separates occupied O  $2p$  states from empty Ti  $3d$  states, as shown in Fig. 5b. The laser pulse has a peak intensity of  $10^{11}$  W/cm<sup>2</sup> with a FWHM of 10 fs which results in a laser fluence of 0.38 mJ/cm<sup>2</sup>.

Fig. 1 shows the change in electronic charge within the MT spheres of O, Ti and the interstitial region for LPL and LH-CPL, whereas no notable Sr-contribution is observed due to the absence of Sr states in the relevant energy region (see Fig. 5(b)). The most prominent feature is a depletion of charge at the O sites and the interstitial region and transfer to the Ti sites. The response to LPL and CPL is similar, except that oscillations in the CPL case are suppressed due to the superposition of two phase-shifted LPL pulses.

Remarkably, the application of the light pulse persistently breaks the cubic symmetry of the SrTiO<sub>3</sub> crystal lattice, lifting the degeneracy between in-plane and out-of-plane O sites, that exhibit a distinct dynamic response. In particular, for LPL a stronger depletion is observed at the out-of-plane oxygen sites. The

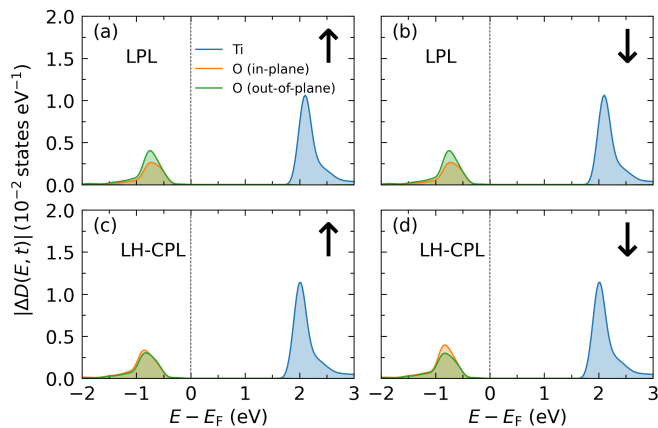


FIG. 2. Changes of the spin- and element-resolved time-dependent density of states (DOS) during the pulse ( $t = 17$  fs) for (a-b) linearly and (c-d) circularly polarized light with laser frequency of  $\hbar\omega = 2.5$  eV with peak intensity  $10^{11}$  W/cm $^2$ . Changes in occupation at negative/positive energies denote initial/final states.

initial and final states involved in this charge transfer are unraveled by the time-dependent density of states  $|\Delta D(E, t)| = |D(E, t) - D(E, 0)|$ , which displays the spin- and element-resolved (absolute) changes in the time dependent occupation of the KS orbitals with respect to the ground state DOS at  $t = 0$ . Fig. 2 shows  $|\Delta D(E, t)|$  at  $t = 17$  fs, right at the maximum of the pulse for LPL and CPL. We observe excitations from O  $2p$  states between  $-1$  and  $-0.5$  eV below  $E_F$  to empty Ti  $3d$  states between  $1.7$  and  $2.3$  eV above  $E_F$ , which is consistent with the laser frequency of  $\hbar\omega = 2.5$  eV. The depletion is distinct for in- and out-of-plane O  $2p$  states, confirming the breaking of symmetry. In contrast to LPL where the two spin channels show identical excitation, there is a noticeable difference between the majority and minority spin for CPL in particular for the O  $2p$  states.

A complementary and rather intuitive way to understand the charge dynamics induced by the laser excitation is offered by the electron density redistribution  $\Delta\rho(\mathbf{r}, t) = \rho(\mathbf{r}, t) - \rho(\mathbf{r}, 0)$  with respect to the initial state. Fig. 3(b-c) display snapshots with charge depletion (red) or accumulation (blue) primarily at the Ti and O sites in the first half ( $t = 10 - 14$  fs) and after the pulse ( $t = 35$  fs).

For LPL (Fig. 3(b)), oscillating positive and negative lobes form at the O and Ti sites along the field direction with opposite orientation at Ti and O sites, signifying a dynamic breaking of inversion symmetry. This dynamic pattern of the electronic clouds is reminiscent of the opposite movement of Ti and O ions in the soft transverse optical TO $_1$  mode (e.g., [61, 62]). The soft TO mode hardens upon application of an electric field [63–65] and may be considered as a signature of the incipient FE of SrTiO $_3$ . An electronic excitation and deformation of the electron density [50] was previously related to the emer-

gence of transient ferroelectricity [47, 48]

A remarkable feature for CPL (Fig. 3(c)) is the rotation of the lobes at the O sites with the electric field, while the positive and negative lobes at the Ti site appear and disappear, predominantly oriented towards the in-plane oxygen ions, following the phase shift between the oscillating  $x$ - and  $y$ -components of the electric field. This establishes an effective circular current that is prone to transfer orbital angular momentum from light to the electronic subsystem, as will be shown in the following. This circular motion of electron density is also expected to generate a circular motion of the ions.

After the decay of the laser pulse, the remaining charge redistribution concentrates at the Ti sites, whereas a depletion of charge persists only at the in-plane O sites for LPL and more pronounced at the out-of-plane oxygen for CPL. At the Ti sites a complex shape emerges with depletion from  $e_g$  orbitals and accumulation into a linear combinations of out-of-plane  $t_{2g}$  orbitals.

The circular motion of the positive and negative lobes of the electron density around the oxygen positions combined with the spin imbalance in the time-resolved DOS implies that CPL can induce a finite magnetization in the otherwise nonmagnetic SrTiO $_3$ , which we elucidate in the following. Fig. 4(a) reveals that a finite transient spin moment  $m_S(t)$  in the order of  $10^{-4}$   $\mu_B$  develops during the pulse for LH-CPL, which subsequently reverses direction reaching twice the magnitude at  $t = 70$  fs. For RH-CPL,  $m_S(t)$  only changes its sign, confirming the helicity dependence. The oscillating behavior of  $m_S(t)$  is a result of the delicate balance of larger, but competing element-specific contributions, as shown in Fig. 4(c): positive magnetization appears at the oxygen sites with a stronger contribution of in-plane oxygen and a pronounced negative contribution at the Ti sites. Initially, this yields a strong positive contribution from O which is not fully compensated by the antiparallel Ti moment. After reaching a maximum toward the end of the pulse (25 fs), all element-specific contributions decrease in magnitude. The spin moment of out-of-plane oxygen eventually changes sign and the negative Ti moment dominates at larger times. Again, for RH-CPL, we obtain the same contributions with opposite sign (not shown), whereas no spin-polarization develops for LPL.

Since the dipole selection rules usually prohibit a direct transfer of angular momentum from the photon to the electron spin, we elucidate the origin of the induced spin moment for CPL with  $\hbar\omega = 2.5$  eV and find that it follows the occurrence of an orbital moment  $m_L(t)$ , which is one order of magnitude larger ( $4 \times 10^{-3}$   $\mu_B$ ), cf. Fig. 4(b).  $m_L(t)$  increases faster than  $m_S(t)$  and reaches its first maximum approximately at the pulse maximum. After this,  $m_L(t)$  preserves a constant magnitude overlaid by characteristic oscillations, originating mainly from the Ti sites, while the dominant contribution arises from in-plane oxygen, as shown in Fig. 4(d). RH-CPL, in turn,

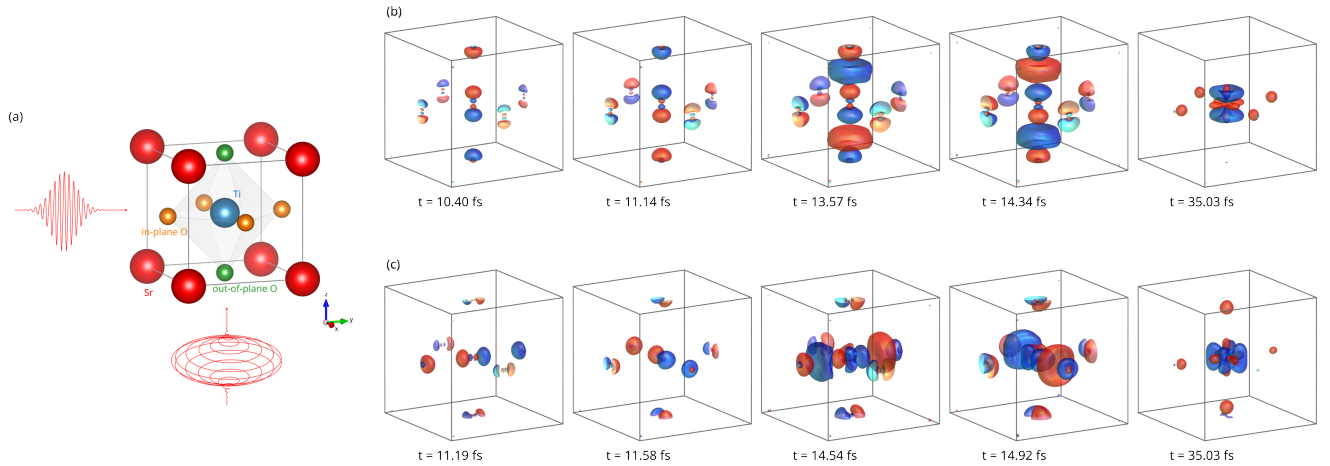


FIG. 3. (a) Graphical illustration of linearly polarized light along the  $z$ -direction and circularly polarized light in the  $xy$ -plane driving the electronic excitation in SrTiO<sub>3</sub>. Snapshots of the time-dependent electron density redistribution  $\Delta\rho(\mathbf{r}, t)$  during and after the laser excitation for (b) linearly and (c) circularly polarized pulse using laser frequency of  $\hbar\omega = 2.5$  eV, FWHM = 10 fs, and laser peak intensity of  $S_{\text{peak}} = 10^{11}$  W/cm<sup>2</sup>. Red and blue colors denote depletion and accumulation of charge, respectively. The isosurface level is  $\pm 2.02 \times 10^{-3} e_0/\text{\AA}^3$ .

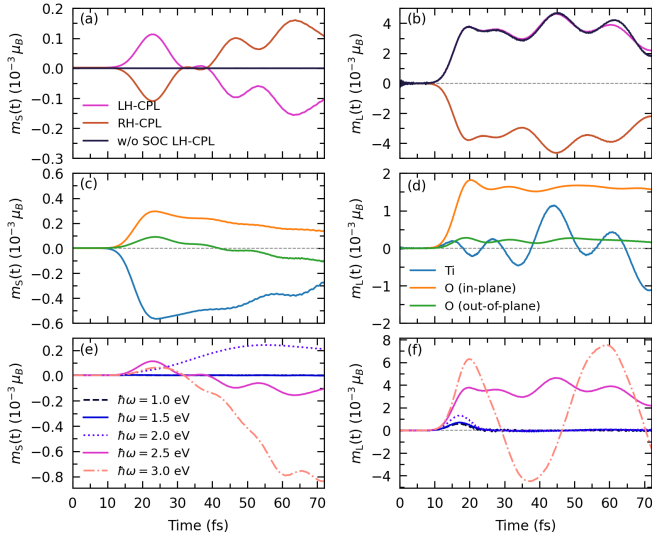


FIG. 4. Light-induced total (a) spin and (b) orbital magnetic moment for CPL with  $\hbar\omega = 2.5$  eV. The exclusion of SOC, denoted by a light blue line in (a) and (b), does not affect the orbital moment but quenches the spin moment. Element-resolved contributions to the laser-induced spin and orbital moment for (c and d) LH-CPL. Comparison of the transient (e) spin and (f) orbital magnetic moment induced by LH-CPL with different laser frequencies ranging from 1.0 eV to 3.0 eV, and  $S_{\text{peak}} = 10^{11}$  W/cm<sup>2</sup>.

(not shown) mirrors exactly the trend with opposite sign.

The evolution of  $m_S(t)$  and  $m_L(t)$  with the photon energy is displayed in Fig. 4(e,f). Laser excitations below the GGA band gap totally quench the spin moment due to the absence of electron excitation but still induce a finite orbital moment solely during the pulse, which follows the Gaussian envelope of the pulse, reaching a maximum

value of  $0.9 \times 10^{-3} \mu_B$ . In contrast, photon energies above the gap yield a persistent  $m_S(t)$  and  $m_L(t)$  even after the pulse. Their shape is, however, not uniform, depending strongly on frequency. For  $\hbar\omega = 2.0$  eV,  $m_L(t)$  decays with the pulse, but induces a notable spin moment which evolves further in time.

*Discussion*—For the optical excitation considered here, only the electrons can follow the rotation of the electric field and contribute to the evolution of transient magnetism, while in the THz experiments of Basini *et al.* [51] the frequency of the electric field oscillation is in the range of phonon modes and the ions can follow the motion of the electron cloud. Urazhdin [58] proposed from a molecular model that the magnetization evolves from the time-dependent modification of hybridization between the orbitals of Ti and the surrounding O stemming from the excitations of circularly polarized phonons connected to the FE soft mode, which causes the periodic driving. The electron density fluctuations in Fig. 3 provide evidence for the orbital-dependent excitation and hybridization and the rotation of induced dipoles around the O sites driven by CPL in the optical frequency range.

A direct comparison to the experimentally measured magnetization of the order of a tenth of  $\mu_B$  [51] might not be meaningful due to the difference in excitation energy and the focus here solely on the electronic degrees of freedom. Still it is worth mentioning that the magnetization predicted from RTTDDFT for CPL excitation in the optical range ( $m_L \sim 10^{-3} \mu_B$ ) is two orders of magnitude higher than the one obtained from the dynamical multiferroicity theory [51] which is in the order of nuclear magneton ( $\mu_N \approx 10^{-4} \mu_B$ ).

Beyond the previous focus primarily on the transfer of spin angular momentum [30–32], we disentangle the

mechanism of angular momentum transfer and the origin of both the spin and orbital contribution. The coincidence between the minima and maxima of oscillations in Fig. 4(a,b) indicates that spin- and orbital degrees of freedom are correlated,  $m_L(t)$  being almost one order of magnitude larger than  $m_S(t)$ . While the role of spin-orbit coupling (SOC) in SrTiO<sub>3</sub> has been questioned previously due to the small SOC splitting of Ti compared to the band gap [58], our results demonstrate the key role of SOC in the transfer of angular momentum from light via the electronic orbital to spin angular momentum. In particular, switching off the spin-orbit coupling (SOC) completely quenches the spin moment, while the induced orbital moment is not affected (cf. Fig. 4a-b.)

The microscopic mechanism identified from the RT-TDDFT results is consistent with the macroscopic IFE [21] also concerning the fact that below a critical field strength the orbital magnetization is proportional to the square of the amplitude of the applied electric field ( $\Delta M_{\text{IFE}} \propto \mathbf{E} \times \mathbf{E}^*$ ) and thus the intensity of the light pulse (see Fig. 7 in the end matter).

To summarize, our RT-TDDFT results demonstrate how ultrafast magnetism can be optically induced in the non-magnetic band insulator SrTiO<sub>3</sub> and uncover the mechanism of angular momentum transfer of light to the electronic orbital angular momentum, which is followed by spin magnetization via SOC. Moreover, our findings indicate that atomic motion is not required to obtain a substantial transient magnetic polarization, instead, circular motion of the orbitally polarized electronic charge cloud around the O ions can be induced by visible or ultraviolet light with frequencies above the band gap. Magnitude and temporal profile of the induced dynamics vary with laser parameters, indicating a tunable control over non-equilibrium states. Our work thus opens a new avenue for manipulating materials as well as their interfaces with time-dependent electromagnetic fields to induce transient magnetization.

*Acknowledgments*—We gratefully acknowledge funding by the Deutsche Forschungsgemeinschaft (DFG, German Research Foundation) within collaborative research center CRC1242 (Project No. 278162697, subproject C02) and computational time at Leibniz Rechenzentrum, project pr87ro and the Center for Computational Sciences and Simulation of the University of Duisburg-Essen on the supercomputer magnitUDE and ampli-tUDE (DFG Grants INST 20876/209-1 FUGG, INST 20876/243-1 FUGG and INST 20876/423-1 FUGG)

---

[1] A. V. Kimel and M. Li, Writing magnetic memory with ultrashort light pulses, *Nat. Rev. Mater.* **4**, 189 (2019).  
 [2] C. D. Stanciu, F. Hansteen, A. V. Kimel, A. Kirilyuk, A. Tsukamoto, A. Itoh, and T. Rasing, All-optical magnetic recording with circularly polarized light, *Phys. Rev.*

*Lett.* **99**, 047601 (2007).  
 [3] S. Mangin, M. Gottwald, C. Lambert, D. Steil, V. Uhlir, L. Pang, M. Hehn, S. Alebrand, M. Cinchetti, G. Malinowski, *et al.*, Engineered materials for all-optical helicity-dependent magnetic switching, *Nat. Mater.* **13**, 286 (2014).  
 [4] C.-H. Lambert, S. Mangin, B. C. S. Varaprasad, Y. Takahashi, M. Hehn, M. Cinchetti, G. Malinowski, K. Hono, Y. Fainman, M. Aeschlimann, *et al.*, All-optical control of ferromagnetic thin films and nanostructures, *Science* **345**, 1337 (2014).  
 [5] E. Beaurepaire, J.-C. Merle, A. Daunois, and J.-Y. Bigot, Ultrafast spin dynamics in ferromagnetic nickel, *Phys. Rev. Lett.* **76**, 4250 (1996).  
 [6] A. Kirilyuk, A. V. Kimel, and T. Rasing, Ultrafast optical manipulation of magnetic order, *Rev. Mod. Phys.* **82**, 2731 (2010).  
 [7] G. Ju, J. Hohlfeld, B. Bergman, R. J. M. van de Veerdonk, O. N. Mryasov, J.-Y. Kim, X. Wu, D. Weller, and B. Koopmans, Ultrafast generation of ferromagnetic order via a laser-induced phase transformation in FeRh thin films, *Phys. Rev. Lett.* **93**, 197403 (2004).  
 [8] A. Kimel, A. Kirilyuk, A. Tsvetkov, R. Pisarev, and T. Rasing, Laser-induced ultrafast spin reorientation in the antiferromagnet TmFeO<sub>3</sub>, *Nature* **429**, 850 (2004).  
 [9] Q. Z. Li, P. Elliott, J. K. Dewhurst, S. Sharma, and S. Shallcross, Ab initio study of ultrafast charge dynamics in graphene, *Phys. Rev. B* **103**, L081102 (2021).  
 [10] M. E. Gruner and R. Pentcheva, Dynamics of optical excitations in a Fe/MgO(001) heterostructure from time-dependent density functional theory, *Phys. Rev. B* **99**, 195104 (2019).  
 [11] E. Shomali, M. E. Gruner, and R. Pentcheva, Anisotropic carrier dynamics in a laser-excited Fe<sub>1</sub>/(MgO)<sub>3</sub>(001) heterostructure from real-time time-dependent density functional theory, *Phys. Rev. B* **105**, 245103 (2022).  
 [12] E. Shomali, M. E. Gruner, and R. Pentcheva, Concerted mechanism of carrier dynamics in laser-excited Fe/(MgO)(001) heterostructures from real-time time-dependent dft, *Adv. Theory Simul.* **7**, 2300319 (2024).  
 [13] J. Šebesta and O. Grånäs, Photo-induced manipulation and relaxation dynamics of Weyl-semimetals, *npj Comput. Mater.* **11**, 219 (2025).  
 [14] H. Bellersen, M. Guerrini, and C. Cocchi, Ultrafast photoexcitation of semiconducting photocathode materials, *Phys. Rev. B* **112**, 024314 (2025).  
 [15] K. Krieger, J. K. Dewhurst, P. Elliott, S. Sharma, and E. K. U. Gross, Laser-induced demagnetization at ultrashort time scales: Predictions of tddft, *J. Chem. Theory Comput.* **11**, 4870 (2015).  
 [16] J. K. Dewhurst, S. Shallcross, P. Elliott, S. Eisebitt, C. v. K. Schmising, and S. Sharma, Angular momentum redistribution in laser-induced demagnetization, *Phys. Rev. B* **104**, 054438 (2021).  
 [17] M. S. Mrudul and P. M. Oppeneer, Ab initio investigation of laser-induced ultrafast demagnetization of L1<sub>0</sub> FePt: Intensity dependence and importance of electron coherence, *Phys. Rev. B* **109**, 144418 (2024).  
 [18] J. K. Dewhurst, P. Elliott, S. Shallcross, E. K. Gross, and S. Sharma, Laser-induced intersite spin transfer, *Nano Lett.* **18**, 1842 (2018).  
 [19] M. S. Mrudul, M. Weißenhofer, and P. M. Oppeneer, Generation of phonons with angular momentum during ultrafast demagnetization, *Phys. Rev. B* **112**, L180407

- (2025).
- [20] L. Pitaevskii, Electric forces in a transparent dispersive medium, *Sov. Phys. JETP* **12**, 1008 (1961).
- [21] P. S. Pershan, J. P. van der Ziel, and L. D. Malmstrom, Theoretical discussion of the inverse Faraday effect, raman scattering, and related phenomena, *Phys. Rev.* **143**, 574 (1966).
- [22] J. P. van der Ziel, P. S. Pershan, and L. D. Malmstrom, Optically-induced magnetization resulting from the inverse Faraday effect, *Phys. Rev. Lett.* **15**, 190 (1965).
- [23] R. Hertel, Theory of the inverse Faraday effect in metals, *J. Magn. Magn. Mater.* **303**, L1 (2006).
- [24] D. Popova, A. Bringer, and S. Blügel, Theory of the inverse Faraday effect in view of ultrafast magnetization experiments, *Phys. Rev. B* **84**, 214421 (2011).
- [25] D. Popova, A. Bringer, and S. Blügel, Theoretical investigation of the inverse Faraday effect via a stimulated raman scattering process, *Phys. Rev. B* **85**, 094419 (2012).
- [26] M. Battiato, G. Barbalinardo, and P. M. Oppeneer, Quantum theory of the inverse Faraday effect, *Phys. Rev. B* **89**, 014413 (2014).
- [27] M. Berritta, R. Mondal, K. Carva, and P. M. Oppeneer, Ab initio theory of coherent laser-induced magnetization in metals, *Phys. Rev. Lett.* **117**, 137203 (2016).
- [28] I. D. Tokman, Q. Chen, I. A. Shereshevsky, V. I. Pozdnyakova, I. Oladyshkin, M. Tokman, and A. Belyanin, Inverse Faraday effect in graphene and Weyl semimetals, *Phys. Rev. B* **101**, 174429 (2020).
- [29] S. Banerjee, U. Kumar, and S.-Z. Lin, Inverse Faraday effect in mott insulators, *Phys. Rev. B* **105**, L180414 (2022).
- [30] M. S. Okyay, A. H. Kulahlioglu, D. Kochan, and N. Park, Resonant amplification of the inverse Faraday effect magnetization dynamics of time reversal symmetric insulators, *Phys. Rev. B* **102**, 104304 (2020).
- [31] O. Neufeld, N. Tancogne-Dejean, U. De Giovannini, H. Hübener, and A. Rubio, Attosecond magnetization dynamics in non-magnetic materials driven by intense femtosecond lasers, *npj Comput. Mater.* **9**, 39 (2023).
- [32] G. Marini and M. Calandra, Theory of ultrafast magnetization of nonmagnetic semiconductors with localized conduction bands, *Phys. Rev. B* **105**, L220406 (2022).
- [33] M. Onoda and S. Tsukahara, The upper limit of thermoelectric power factors in the metal–band-insulator crossover of the perovskite-type oxygen deficient system  $\text{SrTiO}_{3-\delta/2}$ , *J. Phys.: Condens. Matter* **23**, 045604 (2011).
- [34] K. A. Müller and H. Burkard,  $\text{SrTiO}_3$ : An intrinsic quantum paraelectric below 4 K, *Phys. Rev. B* **19**, 3593 (1979).
- [35] J. F. Schooley, W. R. Hosler, and M. L. Cohen, Superconductivity in semiconducting  $\text{SrTiO}_3$ , *Phys. Rev. Lett.* **12**, 474 (1964).
- [36] J. Mannhart and D. G. Schlom, Oxide interfaces—an opportunity for electronics, *Science* **327**, 1607 (2010).
- [37] A. Ohtomo and H. Y. Hwang, A high-mobility electron gas at the  $\text{LaAlO}_3/\text{SrTiO}_3$  heterointerface, *Nature* **427**, 423 (2004).
- [38] A. F. Santander-Syro, O. Copie, T. Kondo, F. Fortuna, S. Pailhès, R. Weht, X. G. Qiu, F. Bertran, A. Nicolaou, A. Taleb-Ibrahimi, P. Le Fèvre, G. Herranz, M. Bibes, N. Reyren, Y. Apertet, P. Lecoeur, A. Barthélémy, and M. J. Rozenberg, Two-dimensional electron gas with universal subbands at the surface of  $\text{SrTiO}_3$ , *Nature* **469**, 189 (2011).
- [39] W. Meevasana, P. D. C. King, R. H. He, S.-K. Mo, M. Hashimoto, A. Tamai, P. Songsirittitigul, F. Baumberger, and Z.-X. Shen, Creation and control of a two-dimensional electron liquid at the bare  $\text{SrTiO}_3$  surface, *Nat. Mater.* **10**, 114 (2011).
- [40] S. Piskunov, E. Heifets, R. Eglitis, and G. Borstel, Bulk properties and electronic structure of  $\text{SrTiO}_3$ ,  $\text{BaTiO}_3$ ,  $\text{PbTiO}_3$  perovskites: an ab initio HF/DFT study, *Comput. Mater. Sci.* **29**, 165 (2004).
- [41] E. Heifets, E. Kotomin, and V. A. Trepakov, Calculations for antiferrodistortive phase of  $\text{SrTiO}_3$  perovskite: hybrid density functional study, *J. Phys. Condens. Matter.* **18**, 4845 (2006).
- [42] R. Wahl, D. Vogtenhuber, and G. Kresse,  $\text{SrTiO}_3$  and  $\text{BaTiO}_3$  revisited using the projector augmented wave method: Performance of hybrid and semilocal functionals, *Phys. Rev. B* **78**, 104116 (2008).
- [43] F. El-Mellouhi, E. N. Brothers, M. J. Lucero, and G. E. Scuseria, Modeling of the cubic and antiferrodistortive phases of  $\text{SrTiO}_3$  with screened hybrid density functional theory, *Phys. Rev. B* **84**, 115122 (2011).
- [44] L. Sponza, V. Véniard, F. Sottile, C. Giorgetti, and L. Reining, Role of localized electrons in electron-hole interaction: The case of  $\text{SrTiO}_3$ , *Phys. Rev. B* **87**, 235102 (2013).
- [45] V. Begum, M. E. Gruner, and R. Pentcheva, Role of the exchange-correlation functional on the structural, electronic, and optical properties of cubic and tetragonal  $\text{SrTiO}_3$  including many-body effects, *Phys. Rev. Mater.* **3**, 065004 (2019).
- [46] V. Begum-Hudde, T. Lojewski, N. Rothenbach, B. Egger, A. Eschenlohr, K. Ollefs, M. E. Gruner, and R. Pentcheva, Nature of excitons in the Ti  $L$  and O  $K$  edges of x-ray absorption spectra in bulk  $\text{SrTiO}_3$  from a combined first principles and many-body theory approach, *Phys. Rev. Res.* **5**, 013199 (2023).
- [47] T. F. Nova, A. S. Disa, M. Fechner, and A. Cavalleri, Metastable ferroelectricity in optically strained  $\text{SrTiO}_3$ , *Science* **364**, 1075 (2019).
- [48] X. Li, T. Qiu, J. Zhang, E. Baldini, J. Lu, A. M. Rappe, and K. A. Nelson, Terahertz field-induced ferroelectricity in quantum paraelectric  $\text{SrTiO}_3$ , *Science* **364**, 1079 (2019).
- [49] D. Shin, S. Latini, C. Schäfer, S. A. Sato, E. Baldini, U. De Giovannini, H. Hübener, and A. Rubio, Simulating terahertz field-induced ferroelectricity in quantum paraelectric  $\text{SrTiO}_3$ , *Phys. Rev. Lett.* **129**, 167401 (2022).
- [50] C. Song, Q. Yang, X. Liu, H. Zhao, C. Zhang, and S. Meng, Electronic origin of laser-induced ferroelectricity in  $\text{SrTiO}_3$ , *J. Phys. Chem. Lett.* **14**, 576 (2023).
- [51] M. Basini, M. Pancaldi, B. Wehinger, M. Udina, V. Unnikandanunni, T. Tadano, M. C. Hoffmann, A. V. Balatsky, and S. Bonetti, Terahertz electric-field-driven dynamical multiferroicity in  $\text{SrTiO}_3$ , *Nature* **628**, 534 (2024).
- [52] D. M. Juraschek, M. Fechner, A. V. Balatsky, and N. A. Spaldin, Dynamical multiferroicity, *Phys. Rev. Mater.* **1**, 014401 (2017).
- [53] D. M. Juraschek, R. M. Geilhufe, H. Zhu, M. Basini, P. Baum, A. Baydin, S. Chaudhary, M. Fechner, B. Flebus, G. Grissonnanche, A. I. Kirilyuk, M. Lemesko, S. F. Maehrlein, M. Mignolet, S. Murakami, Q. Niu, U. Nowak, C. P. Romao, H. Rostami, T. Satoh, N. A.

- Spaldin, H. Ueda, and L. Zhang, Chiral phonons, *Nat. Phys.* **21**, 1532 (2025).
- [54] N. Shabala and R. M. Geilhufe, Phonon inverse Faraday effect from electron-phonon coupling, *Phys. Rev. Lett.* **133**, 266702 (2024).
- [55] R. Merlin, Unraveling the effect of circularly polarized light on reciprocal media: Breaking time reversal symmetry with non-maxwellian magnetic-esque fields, *Phys. Rev. B* **110**, 094312 (2024).
- [56] R. Merlin, Magnetophononics and the chiral phonon misnomer, *PNAS Nexus* **4**, pgaf002 (2025).
- [57] L. Klebl, A. Schobert, M. Eckstein, G. Sangiovanni, A. V. Balatsky, and T. O. Wehling, Ultrafast pseudomagnetic fields from electron-nuclear quantum geometry, *Phys. Rev. Lett.* **134**, 016705 (2025).
- [58] S. Urazhdin, Atomic and interatomic orbital magnetization induced in SrTiO<sub>3</sub> by chiral phonons, *Phys. Rev. B* **111**, 214435 (2025).
- [59] J. K. Dewhurst and S. Sharma, The Elk code, [elk.sourceforge.io](http://elk.sourceforge.io) (2024).
- [60] J. P. Perdew, A. Ruzsinszky, G. I. Csonka, O. A. Vydrov, G. E. Scuseria, L. A. Constantin, X. Zhou, and K. Burke, Restoring the density-gradient expansion for exchange in solids and surfaces, *Phys. Rev. Lett.* **100**, 136406 (2008).
- [61] U. Aschauer and N. A. Spaldin, Competition and cooperation between antiferrodistortive and ferroelectric instabilities in the model perovskite SrTiO<sub>3</sub>, *J. Phys. Condens. Matter.* **26**, 122203 (2014).
- [62] M. Kozina, M. Fechner, P. Marsik, T. van Driel, J. M. Glowia, C. Bernhard, M. Radovic, D. Zhu, S. Bonetti, U. Staub, and M. C. Hoffmann, Terahertz-driven phonon upconversion in SrTiO<sub>3</sub>, *Nat. Phys.* **15**, 387 (2019).
- [63] P. A. Fleury, J. F. Scott, and J. M. Worlock, Soft phonon modes and the 110° K phase transition in SrTiO<sub>3</sub>, *Phys. Rev. Lett.* **21**, 16 (1968).
- [64] I. A. Akimov, A. A. Sirenko, A. M. Clark, J.-H. Hao, and X. X. Xi, Electric-field-induced soft-mode hardening in SrTiO<sub>3</sub> films, *Phys. Rev. Lett.* **84**, 4625 (2000).
- [65] H. Jacobsen, M. Barthkowiak, T. Weber, U. Stuhr, B. Roessli, C. Niedermayer, and U. Staub, Phonon dispersion of quantum paraelectric SrTiO<sub>3</sub> in electric fields, *Phys. Rev. B* **110**, 054302 (2024).

## End Matter

Ground state and time-dependent electronic structure was obtained using the five atom cubic primitive cell of SrTiO<sub>3</sub> with a lattice constant of 3.894 Å [45]. We chose muffin-tin (MT) radii of 1.376 Å, 1.097 Å, and 0.823 Å for Sr, Ti, and O, respectively. The plane-wave cutoff parameter,  $RK_{\max}$ , was set to 8. We employed a  $\mathbf{k}$ -mesh of  $10 \times 10 \times 10$  to sample the Brillouin zone for both the ground-state and the time-dependent calculations. As shown in Fig. 5(a) and consistent with previous work [42, 45], SrTiO<sub>3</sub> is a band insulator with the valence band maximum (VBM) located at  $R$  and the conduction band minimum (CBM) at  $\Gamma$ , resulting in an indirect ( $R - \Gamma$ ) and direct band gap ( $\Gamma - \Gamma$ ) of 1.81 eV and 2.16 eV with the PBEsol exchange correlation functional, respectively. Moreover, the projected density of states in Fig. 5(b) shows that the valence band is mostly comprised of O

$2p$  states, whereas the conduction band minimum has Ti  $t_{2g}$  character. Many body effects (GW+BSE) [44, 45] are necessary to obtain the experimental band gap of 3.2 eV, but the shape and sequence of relevant bands is preserved.

For the time-propagation a time-step size of  $\Delta t = 0.726$  attoseconds was selected. Since phonons are not expected to be excited at the photon energies in the optical range considered here, we concentrate solely on the electronic effects.

The time-dependent density of states at a particular time  $t$ ,  $D(E, t)$ , is calculated using [18]:

$$D(E, t) = \sum_{i=1}^{\infty} \int_{BZ} \delta(E - \epsilon_{i\mathbf{k}}) g_{i\mathbf{k}}(t) \quad (2)$$

with

$$g_{i\mathbf{k}}(t) = \sum_j n_{j\mathbf{k}} \int d^3r \psi_{i\mathbf{k}}^*(\mathbf{r}, 0) \psi_{j\mathbf{k}}(\mathbf{r}, t) \quad (3)$$

where  $n_{j\mathbf{k}}$  is the occupation number of the  $j^{\text{th}}$  orbital and  $\psi_{i\mathbf{k}}(\mathbf{r}, 0)$  is the ground state Kohn-Sham orbital.

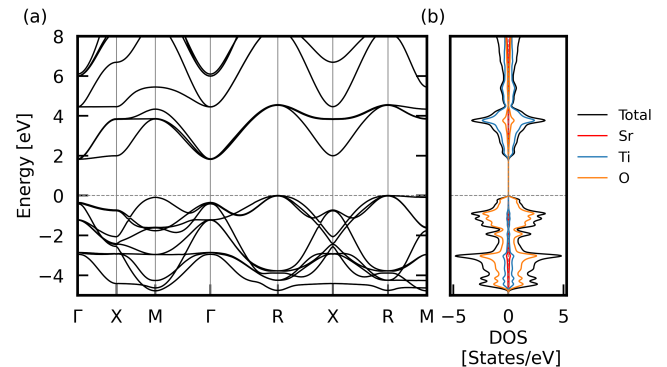


FIG. 5. (a) Electronic band structure along the high-symmetry directions and (b) projected density of states (PDOS) of SrTiO<sub>3</sub> obtained with the PBEsol exchange-correlation functional.

Changes in the time-dependent total Kohn-Sham energy during and after the pulse give insight into the material's response to the penetrating light wave indicating transient and permanent changes to the state of the material. Our simulations (cf. Fig. 6) show a persistent energy uptake of 38 meV/f.u. after the pulse for both LPL and CPL with  $\hbar\omega = 2.5$  eV beyond the GGA band gap, while the energy (nearly) returns to the initial level for  $\hbar\omega = 1.5$  eV, below the band gap of SrTiO<sub>3</sub> shown in Fig. 6. The change in the energy of the system during the pulse corresponds to the material's response to the penetrating light wave. Interestingly, the change in the total energy at the maximum of the pulse envelope is larger for photon energies below the gap compared to the absorbing case. As the material is transparent to

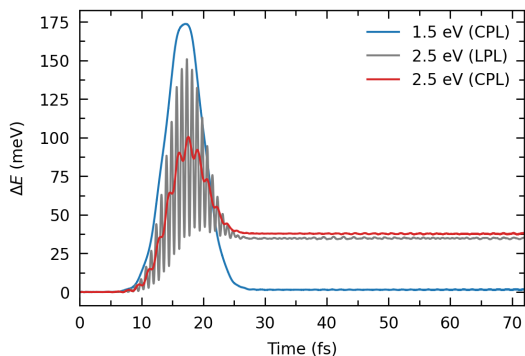


FIG. 6. The time evolution of changes in the total energy of the electronic system upon laser excitation for LPL and CPL with frequency of  $\hbar\omega = 2.5$  eV and CPL with laser frequency below the band gap ( $\hbar\omega = 1.5$  eV) with constant FWHM = 10 fs and laser peak intensity  $S_{\text{peak}} = 10^{11}$  W/cm<sup>2</sup>

light with this frequency, the energy and other transient modifications are restored after the pulse.

From the theory of IFE one expects that the induced magnetization is proportional to the square of the applied electric field ( $\Delta M_{\text{IFE}} \propto \mathbf{E} \times \mathbf{E}^*$ ) and thus the intensity of the light pulse. To confirm this we varied the peak power density  $S_{\text{peak}}$  of the light pulse, which is proportional to the squared amplitude of its electric field, by two orders of magnitude. The impact on the spin and orbital magnetization is shown in Fig. 7(a,b), respectively. Indeed, we find that both spin and orbital moments increase nearly proportionally by a factor of 10, when we increase  $S_{\text{peak}}$  from  $10^{10}$  W/cm<sup>2</sup> to  $10^{11}$  W/cm<sup>2</sup>.

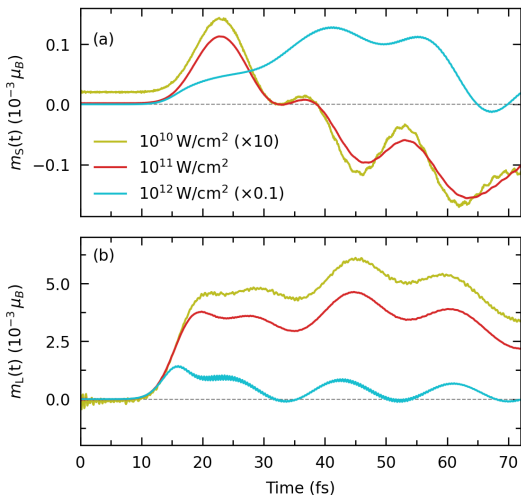


FIG. 7. Light-induced spin and orbital magnetic moment for circularly pulses with photon energy  $\hbar\omega = 2.5$  eV with different laser peak intensity of  $10^{10}$  W/cm<sup>2</sup>,  $10^{11}$  W/cm<sup>2</sup>, and  $10^{12}$  W/cm<sup>2</sup>, shown in olive, red, and cyan line, respectively.

In the strong laser regime at  $S_{\text{peak}} = 10^{12}$  W/cm<sup>2</sup> the linear proportionality of the laser-induced magnetization relative to the laser intensity starts to break down. This becomes apparent from the magnitude and dynamics of the spin moment in Fig. 7(a), which shows a slower increase and remains positive up to  $t = 65$  fs. The dynamics of the laser-induced orbital moment in the strong laser regime is qualitatively similar to the lower values of  $S_{\text{peak}}$  albeit with a significantly lower magnitude [Fig. 7(b)]. Thus, increasing the laser intensity beyond a critical threshold may become detrimental for the induced magnetization.